

Radar imaging of Asteroid 7 Iris

S.J. Ostro^{a,1}, C. Magri^{b,*}, L.A.M. Benner^a, J.D. Giorgini^a, M.C. Nolan^c, A.A. Hine^c, M.W. Busch^d, J.L. Margot^e

^aJet Propulsion Laboratory, California Institute of Technology, Pasadena, CA 91109, USA

^bUniversity of Maine at Farmington, 173 High Street – Preble Hall, Farmington, ME 04938, USA

^cArecibo Observatory, HC3 Box 53995, Arecibo, PR 00612, USA

^dDivision of Geological and Planetary Sciences, California Institute of Technology, MC 150-21, Pasadena, CA 91125, USA

^eDepartment of Earth and Space Sciences, University of California, Los Angeles, 595 Charles Young Drive East, Box 951567, Los Angeles, CA 90095, USA

ARTICLE INFO

Article history:

Received 26 June 2009

Revised 10 October 2009

Accepted 7 November 2009

Available online 24 November 2009

Keywords:

Asteroids

Radar observations

ABSTRACT

Arecibo radar images of Iris obtained in November 2006 reveal a topographically complex object whose gross shape is approximately ellipsoidal with equatorial dimensions within 15% of 253×228 km. The radar view of Iris was restricted to high southern latitudes, precluding reliable estimation of Iris' entire 3D shape, but permitting accurate reconstruction of southern hemisphere topography. The most prominent features, three roughly 50-km-diameter concavities almost equally spaced in longitude around the south pole, are probably impact craters. In terms of shape regularity and fractional relief, Iris represents a plausible transition between ~ 50 -km-diameter asteroids with extremely irregular overall shapes and very large concavities, and very much larger asteroids (Ceres and Vesta) with very regular, nearly convex shapes and generally lacking monumental concavities.

© 2009 Elsevier Inc. All rights reserved.

1. Introduction

Many near-Earth asteroids (NEAs) have been imaged with delay-Doppler radar, and 3D shape models have been published for 20 of them (e.g., tabulation by Ostro et al. (2002) and references therein). However, echoes from main-belt asteroids (MBAs) are much weaker than echoes from closely approaching NEAs due to the inverse-fourth-power dependence of echo strength on distance. Shepard et al. (2008) presented delay-Doppler images for 16 Psyche and 21 Lutetia as well as a 3D model based on Doppler-resolved echo spectra of 129 Antigoné. However, 216 Kleopatra (Ostro et al., 2000) is the only MBA for which delay-Doppler images and shape reconstruction results have been published.

The accuracy of radar-based shape reconstruction (e.g., Hudson and Ostro, 1994) depends on the echo's signal-to-rms-noise ratio (SNR) and orientational coverage as well as the target's shape and spin state, in a manner that has been explored and calibrated by extensive numerical experiments and by laboratory simulations using clay models and a laser as a proxy for a radar (Andrews et al., 1995) as well as in inversion of radar data for asteroids for which

optical images exist (Ostro et al., 2005). Unambiguous, global, 3D reconstruction from a radar image sequence requires sufficient rotation-phase coverage as well as latitude coverage at least $\pm 20^\circ$ from the equator to overcome the north-south delay-Doppler ambiguity.

The 0.85-AU close approach of 7 Iris in November 2006 offered the best MBA asteroid radar opportunity to date, yielding Arecibo *single-date* SNRs of about 500, more than twice the *multi-date* total SNR of all the Kleopatra images combined. Here we report the results of our Iris observations.

2. Prior information about Iris

Iris is one of the brightest objects in its VIS/IR spectroscopic class S4, which corresponds to an olivine-orthopyroxene (Ca-poor) mineralogy (Gaffey et al., 1993) offering a good match to ordinary chondrites (possibly L chondrites; Gaffey et al., 2002) which constitute more than 70% of meteorite falls (Vernazza et al., 2008). Farinella et al. (1993) characterized Iris as having a relatively high meteorite-delivery efficiency due to its proximity to the 3:1 mean-motion resonance with Jupiter, which is thought to be a major dynamical conduit from the main belt to Earth-crossing orbits. That study and long-term orbit integrations by Migliorini et al. (1997) suggest that several percent of impact ejecta from Iris might reach the resonance, so some of our ordinary chondrites may be pieces of Iris. This connection contributed to selection of Iris as the target of a University of Arizona/Brown University/JPL mission study, the AMBASSADOR (A Main Belt Asteroid Seismic study and

* Corresponding author. Fax: +1 207 778 7365.

E-mail address: magri@maine.edu (C. Magri).

¹ Deceased. Steve Ostro led the radar observations of 7 Iris, played the principal role in the analysis of those data, and created several drafts of this paper, nearly bringing the process to completion before his untimely death on December 15, 2008. His determination in the face of illness was remarkable. The second author then supervised the completion of the manuscript (primarily by composing Fig. 1 and the Appendix) and handled the editorial process.

Sample Acquisition to Determine meteorite ORIGins) mission (Turtle et al., 1999).

Spectrophotometry indicates that the asteroid is mineralogically homogeneous (Migliorini et al., 1997). However, optical lightcurves have been interpreted to show noncontiguous high-albedo regions (Hoffmann and Geyer, 1993), optical polarimetry shows “remarkable” variations and implies a variegated surface microstructure (Broglia and Manara, 1990), and radar echo spectra from 1984 have spikes within narrow regions of rotation phase that suggest at least one flat, normally oriented region tens of kilometers across (Mitchell et al., 1995). Coarse-resolution Goldstone-VLA images of Iris (de Pater et al., 1994) showed departure from an axisymmetric shape. Mitchell et al. (1995) used radar spectra from 1980, 1984, and 1991 to define an ellipsoid approximation (Table 1) consistent with the radar data and optical lightcurves.

IRAS observations of Iris yielded a radiometric diameter of 200 ± 10 km (Tedesco et al., 2002), but this analysis assumed a spherical asteroid and the Standard Thermal Model. Departures from these idealizations could bias the estimate, especially for an object like Iris, whose pole is close enough to the ecliptic to produce major seasonal variations in temperature. Magri et al. (1999) reviewed available radar and lightcurve information and adopted the Mitchell et al. (1995) reference ellipsoid to interpret radar results obtained in 1980, 1984, 1991, and 1995.

Kaasalainen et al. (2002) used lightcurves to construct a convex polyhedral model with equivalent ellipsoid axis ratios of $a/b = 1.2$ and $b/c = 1.0$ and which they describe as “a rather roughly cut spherical body ... probably some of the rough cuts seen in the images should be attributed to albedo markings (a flat large facet corresponding to a brighter albedo spot, and a sharper edge corresponding to a darker region ...).” Magri et al. (2007a) altered the Magri et al. (1999) reference ellipsoid in consideration of the Kaasalainen et al. (2002) results; uncertainties given for the Magri et al. (1999, 2007) reference ellipsoids overlap (Table 1).

The most thorough set of stellar occultation chords obtained for Iris, from 2005 February 27 (RASNZ, 2006), was modeled by an elliptical profile, but their fit converged “to many potential solutions with major axes between about 200 and 340 km, so it is not possible to make any more definitive statement about the major and minor axes of Iris.”

In preparation for the analysis of our 2006 imaging data, we explored in great detail the lightcurve data analyzed by Kaasalainen et al. (2002) and concluded that those authors’ description of their lightcurve data set as “not a very good one, suffering from bad timings, ambiguous composites, etc.” was not overstated, and in particular that incorporation of lightcurve data in our shape inversion was not warranted. We used the reference ellipsoid adopted by Mitchell et al. (1995) and Magri et al. (1999) as the starting point for the shape inversion calculations described below.

3. Observations

We completed 23 transmit–receive cycles (runs) during our tracks on 2006 November 11–15 (Table 2). Each run took about 28 min (14 min each for transmit and receive). We transmitted a monochromatic 2380-MHz (12.6-cm) circularly polarized signal. The transmitted waveform was a non-repeating binary-phase-coded continuous wave with a 70- μ s “baud” (the basic time-modulation interval between phase-flip or no-phase-flip decisions). Details of the non-repeating “long code” observing method are provided in Appendix A. We received echo power both in the circular polarization sense opposite that transmitted (OC) and in the same sense (SC). As is typical for MBAs, the OC echo from Iris was much stronger than the SC echo, indicating the dominance of single reflections from surface elements that are large compared to the wavelength; as a result we used only the OC data for our shape inversion. Reception consisted of sampling twice per baud, cross-correlation with the transmitted code (decoding), and Fourier transformation of the signal in each range cell to produce a delay-Doppler image with 10.2-Hz frequency resolution.

Each run produced one such image, which we vignetted to 50 range rows (separated by 35 μ s, or 5.25 km, but with an intrinsic range resolution of twice that) by 99 frequency columns. The conversion from frequency to length depends on the object’s instantaneous spin state; our inversion of images did not refine our adopted spin state (Table 1), for which 10.2 Hz corresponds to 4.0 km. If the row and column indices are counted from one, then if the delay-Doppler prediction ephemeris were perfect, echo from Iris’ center-of-mass would fall in row 532 and column 50. Our modeling revealed range corrections on November 11 and 15 of 18.9 ± 15 km and

Table 1
Model characteristics.

| Model | Mitchell et al. (1995) and Magri et al. (1999) reference ellipsoid | Magri et al. (2007a) reference ellipsoid | This work, vertex model with 2586 vertices and 5168 facets |
|---|---|---|---|
| Principal axis extents (km) | | | |
| <i>x</i> | 260 \pm 39 | 227 \pm 25 | 253 \pm 38 |
| <i>y</i> | 220 \pm 33 | 189 \pm 21 | 228 \pm 34 |
| <i>z</i> | 155 \pm 23 | 189 \pm 21 | 193 \pm 39 |
| Axis ratios | | | |
| <i>x/y</i> | 1.2 \pm 0.3 | 1.2 \pm 0.2 | 1.1 \pm 0.2 |
| <i>y/z</i> | 1.4 \pm 0.3 | 1.0 \pm 0.2 | 1.2 \pm 0.2 |
| Equivalent diameter (km) | 207 \pm 22 | 201 \pm 20 | 208 \pm 35 |
| Volume (10^6 km ³) | 4.6 \pm 2.1 | 4.2 \pm 1.4 | 4.7 \pm 2.3 |
| Convex envelope volume (10^6 km ³) | | | 5.0 |
| Pole ecliptic longitude, latitude (°) | 15 \pm 5, +25 \pm 15 | 20, +10 | 15 \pm 5, +25 \pm 15 |
| Rotation period (h) | 7.138 | 7.1388 | 7.1388 \pm 0.0001 |

Note: The two left-hand columns give characteristics of the reference ellipsoids adopted by Magri et al. (1999, 2007a) for their analyses of radar spectra. The right-hand column gives characteristics of the vertex model presented in this paper, whose development used the Magri et al. (1999) reference ellipsoid as initial conditions. Uncertainties listed for reference ellipsoids are those given in the cited papers or are derived directly from them. Uncertainties listed for our vertex model are intended to be conservative estimates of standard errors. Each model is described with Cartesian body-fixed coordinates with rotation about the *z* axis. The scattering law of our nominal solution is $d\sigma/dA \sim \cos^{2c} \theta$, where σ is radar cross section, A is surface area, and θ is angle of incidence. If a Parker (1973) probability density function is assumed to describe the distribution of surface slopes with respect to the model shape, then this law corresponds to an adirectional root-mean-square slope $S_{rms} = \tan^{-1}[C^{-1/2}]$ of unresolved facets relative to the reconstructed shape (Mitchell et al., 1995). Our estimation yields C equal to about 2.83, which corresponds to a value of about 31° for the slope, comparable to corresponding values for other main-belt asteroids (Mitchell et al., 1996) but about five times as large as lunar values (Simpson and Tyler, 1982) and a little smaller than typical angles of repose expected for regolith.

21.7 ± 15 km to the pre-experiment range prediction of JPL Iris orbit solution 69; this is about one-sixth of an Iris radius.

Six of our 23 delay-Doppler images are displayed in Fig. 1. A convex-definite target would produce echoes with a simple concave-downward structure in delay-Doppler space, perhaps with clumps of especially bright pixels indicating the presence of smooth, flat surface regions that are facing directly toward the radar. Such glints are certainly present in these images but we also see structure in the leading edge and, especially, behind the leading edge. The latter features demonstrate that Iris must be topographically complex, with significant concavities located away from the apparent equator.

4. Shape estimation

Our SHAPE modeling software, described most thoroughly by Magri et al. (2007b; see Appendix A), uses least squares to estimate

Table 2
Iris images.

| | 2006 November date | Receive start (hh mm ss) | East longitude (°) | Latitude (°) | Rotation phase (°) |
|-------|--------------------------|--------------------------------|-----------------------|--------------|-----------------------|
| | 11 | 3 38 30 | 83.74 | −48.78 | 276.26 |
| | 11 | 4 06 44 | 60.01 | −48.78 | 299.99 |
| | 11 | 4 34 58 | 36.27 | −48.79 | 323.73 |
| | 11 | 5 03 12 | 12.54 | −48.79 | 347.46 |
| | 11 | 5 31 26 | 348.8 | −48.79 | 11.20 |
| | 12 | 3 50 30 | 303.09 | −48.93 | 56.91 |
| | 12 | 4 18 44 | 279.36 | −48.94 | 80.64 |
| | 12 | 4 46 58 | 255.62 | −48.94 | 104.38 |
| | 12 | 5 15 12 | 231.89 | −48.94 | 128.11 |
| | 13 | 3 12 05 | 204.82 | −49.08 | 155.18 |
| | 13 | 3 40 19 | 181.09 | −49.08 | 178.91 |
| | 13 | 4 08 33 | 157.35 | −49.08 | 202.65 |
| | 13 | 4 36 47 | 133.62 | −49.08 | 226.38 |
| | 13 | 5 05 01 | 109.88 | −49.09 | 250.12 |
| | 14 | 3 07 15 | 78.32 | −49.23 | 281.69 |
| | 14 | 3 35 29 | 54.58 | −49.23 | 305.42 |
| | 14 | 4 03 43 | 30.84 | −49.23 | 329.16 |
| | 14 | 4 31 57 | 7.11 | −49.24 | 352.89 |
| | 14 | 5 00 11 | 343.37 | −49.24 | 16.63 |
| | 15 | 3 36 30 | 283.16 | −49.37 | 76.84 |
| | 15 | 4 04 46 | 259.39 | −49.38 | 100.61 |
| | 15 | 4 33 02 | 235.63 | −49.38 | 124.37 |
| | 15 | 5 01 18 | 211.87 | −49.38 | 148.13 |
| Index | | | | | |
| 1 | 11 | 5 31 26 | 348.80 | −48.79 | 11.20 |
| 2 | 14 | 5 00 11 | 343.37 | −49.24 | 16.63 |
| 3 | 12 | 3 50 30 | 303.09 | −48.93 | 56.91 |
| 4 | 15 | 3 36 30 | 283.16 | −49.37 | 76.84 |
| 5 | 12 | 4 18 44 | 279.36 | −48.94 | 80.64 |
| 6 | 15 | 4 04 46 | 259.39 | −49.38 | 100.61 |
| 7 | 12 | 4 46 58 | 255.62 | −48.94 | 104.38 |
| 8 | 15 | 4 33 02 | 235.63 | −49.38 | 124.37 |
| 9 | 12 | 5 15 12 | 231.89 | −48.94 | 128.11 |
| 10 | 15 | 5 01 18 | 211.87 | −49.38 | 148.13 |
| 11 | 13 | 3 12 05 | 204.82 | −49.08 | 155.18 |
| 12 | 13 | 3 40 19 | 181.09 | −49.08 | 178.91 |
| 13 | 13 | 4 08 33 | 157.35 | −49.08 | 202.65 |
| 14 | 13 | 4 36 47 | 133.62 | −49.08 | 226.38 |
| 15 | 13 | 5 05 01 | 109.88 | −49.09 | 250.12 |
| 16 | 11 | 3 38 30 | 83.74 | −48.78 | 276.26 |
| 17 | 14 | 3 07 15 | 78.32 | −49.23 | 281.69 |
| 18 | 11 | 4 06 44 | 60.01 | −48.78 | 299.99 |
| 19 | 14 | 3 35 29 | 54.58 | −49.23 | 305.42 |
| 20 | 11 | 4 34 58 | 36.27 | −48.79 | 323.73 |
| 21 | 14 | 4 03 43 | 30.84 | −49.23 | 329.16 |
| 22 | 11 | 5 03 12 | 12.54 | −48.79 | 347.46 |
| 23 | 14 | 4 31 57 | 7.11 | −49.24 | 352.89 |

Note: Images used for our shape analyses are listed with UT receive start epochs and corresponding subradar east longitude, latitude, and rotation phase (west longitude), chronologically in the top block and in order of increasing rotation phase (as in Fig. 2) in the bottom block. Each run integrated echoes over about 12° of rotation phase.

a physical model from radar delay-Doppler images, radar Doppler spectra, optical lightcurves, and/or plane-of-sky optical images. The basic strategy is to proceed from a simple shape representation (an ellipsoid) to a spherical-harmonics representation, and finally to a polyhedral representation defined by some number of vertices that is adequate to capture the structural information in the data.

At each stage, one may have to do grid searches over parameter space – for example, carrying out modeling runs for each of a series of model pole latitudes and longitudes covering a significant solid angle on the sky – to ensure that global chi-square minima are identified reliably for key model parameters. One also must experiment with effects of initial conditions, parameter step sizes, and convergence criteria. For radar images, parameters are needed for corrections to the prediction ephemerides for time delay and Doppler frequency that were used for each observation; radar spectra require parameters for Doppler corrections. (Magri et al. (2007a,b) fully describe the observing procedures and data reduction methods used for delay-Doppler imaging and for Doppler-only spectroscopy.) There are also parameters for radar and/or optical scattering. Depending on the nature of the data and the model, there can be various kinds of coupling between parameters, leading to a complex multi-dimensional parameter space even for ellipsoid models. SHAPE uses constrained least squares, penalizing unacceptable structural or dynamical properties of the model (such as large surface spikes) via functions whose weights determine the pressure of the penalties on the objective function being minimized, that is, how the fit is being constrained. Hence a great deal of the shape modeling process requires subjective judgment calls.

For Iris, visual inspection of the images and our initial round of SHAPE experiments confirmed that the Magri et al. (1999) reference ellipsoid was a valid starting point for our modeling. We held the spin vector constant and applied dynamical and structural penalty constraints that effectively kept the gross characteristics of the model close to those of the reference ellipsoid.

5. Modeling results

Each row in Fig. 2 has four 350-by-350-km frames showing the “fit” image synthesized from our nominal vertex model, the corresponding data image, the residuals left when the data image is subtracted from the model image, and a plane-of-sky view of the shape model. The rows are in order of increasing rotation phase (decreasing east longitude); see Table 2.

The Iris images are complex, revealing that the parts of Iris seen by the radar are highly non-convex. The delay-Doppler dispersions of the images are consistent with the size and moderately regular overall shape of the reference ellipsoid, but the contours of the leading edges and the image structure require complex, dramatic topography.

The matches between data images and fit images are very good, with root reduced chi-square equal to 1.08 for the whole data set and between 1.04 and 1.17 for individual frames, indicating a fair degree of accuracy in the reconstruction of Iris’ topography. The residuals are most likely due to a combination of: (i) scattering-law heterogeneities that depart from our (homogeneous and azimuthally isotropic) model radar scattering law and (ii) the presence of topography that is too severe for our modeling to reproduce because of our conservative weighting of penalty functions that suppress dramatic topography. In choosing these weights, we preferred to err on the side of failing to reproduce the most severe aspects of Iris’ actual topography than to err on the side of showing structure that is an artifact of the shape inversion.

We now compare our results with those of Mitchell et al. (1995), who analyzed 1984 Arecibo continuous-wave (CW = Doppler-only)

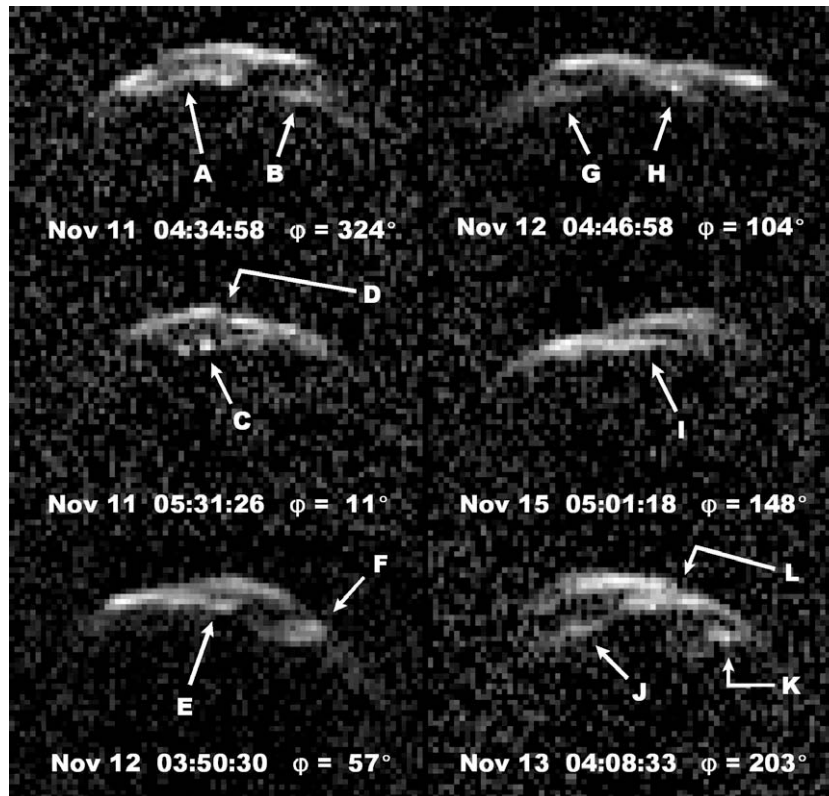


Fig. 1. Collage of selected radar images of Iris, covering two-thirds of a rotation at roughly equal phase intervals. Each image is labeled by its UT receive start epoch and its rotation phase (see Table 2). Delay increases downward (i.e., the radar illuminates the target from above) and Doppler increases rightward. Pixel resolution is $35 \mu\text{s} \times 10.2 \text{ Hz}$. Each image has been scaled separately in brightness so that its strongest pixel appears bright white; the absolute strengths of these peak pixels are in the approximate proportions (top to bottom and left to right) 1.0:1.1:2.1:1.5:1.1:1.0. Labels indicate structure in the target's leading edge (features D, F, and L) and especially behind the leading edge (features A–C, E, and G–K); these features demonstrate that Iris must have significant surface concavities, as a convex-definite asteroid would produce simple “inverted U” echoes.

spectra of Iris and reported the presence of a reflectivity spike centered at -305 Hz and persisting over only a narrow range of rotation phase. They interpreted this feature as being a quasispecular glint from a flat surface facet at least 25 km across. Four other CW experiments in 1980, 1991, 1995, and 2000 (see Mitchell et al. and also the online supplementary material for Magri et al. (2007a)) did not yield convincing rotation-resolved spikes, although in some cases this may be due to weak SNR or incomplete rotational coverage.

We did not obtain any CW spectra in 2006, so instead we have summed our delay-Doppler images over delay to produce synthetic spectra. When we do this for consecutive images 13–15 in Fig. 2c we see a spike in image 14 that is not present at adjacent rotation phases. (We do not display the synthetic spectra here but the transient spike is visible in Fig. 2c as the bright spot on the right [positive-Doppler] side of the “obs” frame for image 14.) This spike is similar to that seen in the 1984 data, but since it is centered at $+175 \text{ Hz}$, it must result from a different surface feature than that inferred by Mitchell et al. The difference in subradar latitude (-22° in 1984 and -49° in 2006) presumably accounts for these results. Our Iris model does not predict a strong spike in 1984, but then it does not reproduce the 2006 glint especially well either: the bright spot in the “res” frame for image 14 in Fig. 2c represents an 18-sigma residual. We often find that strong, transient glints are not well represented by our models; for example, this was the case for 1580 Betulia (Magri et al., 2007b; see Section 4.4). As was mentioned earlier, this may be a consequence of our conservative approach to the modeling process, as we are reluctant to invoke highly angular topography or to employ an inhomogeneous scattering law.

Fig. 3 shows principal-axis views of our nominal model and Table 1 lists model parameters and our estimated standard errors. Our extensive modeling experiments established that several factors preclude estimation of key aspects of Iris' global 3D shape at an acceptable level of accuracy. First, although our rotational phase coverage is thorough, the subradar latitude during the imaging stayed between -48° and -50° , so much of the asteroid was not seen at all. In Fig. 3, areas colored yellow were never seen at incidence angles less than 60° , ensuring that their contributions to the signal were weak or nonexistent. Echo spectra from other years and optical lightcurves offer information that in principle can help to compensate for this deficit in geometric leverage, but in practice the degree to which this deficit can be quantitatively overcome in this manner for Iris is negligible. The northern hemisphere extent of the model is constrained by our dynamical penalties; we assume principal-axis rotation and uniform-density and force the model's principal axes to coincide with its three body-fixed coordinate axes. The north polar topography is an artifact of the overall fitting process.

The uncertainty in Iris' pole direction is of order 10° . The conversion factor relating kilometers to hertz at the Arecibo 2380-MHz transmitter frequency is $\text{KM}/\text{HZ} = \text{PHR}/(27.7 \cos(\text{LAT}))$, where PHR is the object's spin period in hours and LAT is the subradar latitude. This cosine changes rapidly for high absolute values of LAT, which means that there is a very strong coupling between estimations of the asteroid's equatorial size and the pole direction. (The asteroid's polar extent is even more weakly constrained because of the nature of the delay-Doppler projection.) The strong covariance between these characteristics undermines the uniqueness in estimating either.

Compounding this problem is the fact that the radar angular scattering law is coupled to the other two factors. With enough geometric leverage and diverse plane-of-sky views, covariances can be shrunk so efficiently that pole direction, target dimensions, and radar scattering law parameters can be estimated very precisely. Not so with Iris. Hence the large uncertainties assigned to the model's dimensions in Table 1. Our Iris model does not have

the *global* accuracy of previously published radar-derived 3D models.

Iris' shape does not display pronounced global-scale concavities and hence is not poorly approximated by an ellipsoid. If it had an extremely non-convex shape, then its intrinsic geometric nature might allow reliable definition of that shape despite limited orientational coverage. Crudely, this is why we were able to invert the

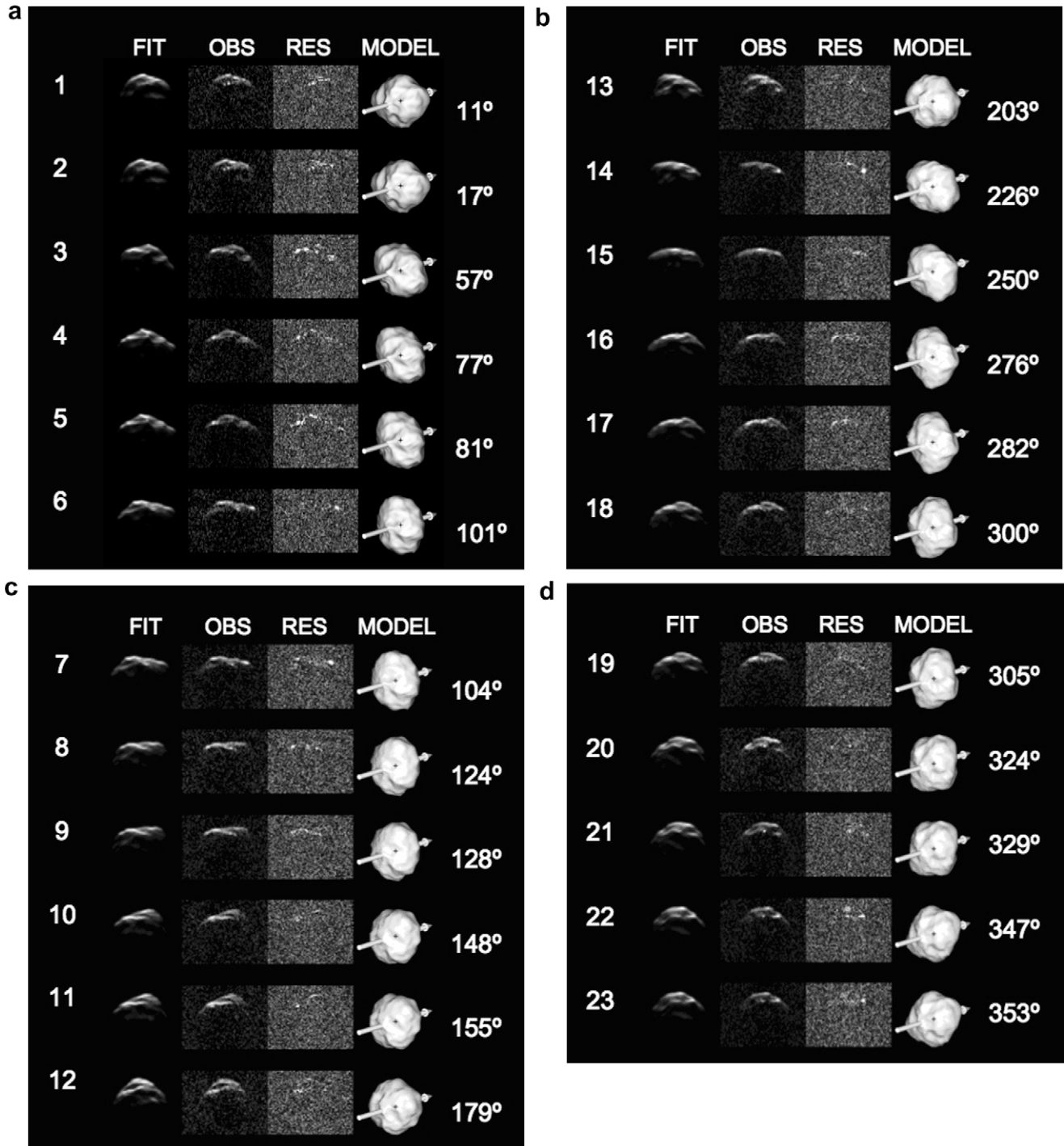


Fig. 2. (abcd) Model estimation results. Each row has 350-by-350-km frames showing (left to right) a “fit” image synthesized from our nominal vertex model, the data image, the absolute values of the residuals left when the latter is subtracted from the former, and a plane-of-sky view of the shape model. These frames' dimensions differ from the original data image frames, whose range-Doppler extents are $([50 \text{ pixels} \times 5.25 \text{ km/pixel}] = 262.5 \text{ km})$ by $([99 \text{ pixels} \times 4 \text{ km/pixel}] = 396 \text{ km})$. Each frame is centered on the model center-of-mass (COM), shown as a plus sign (+) in the right-hand column. In the delay-Doppler images, range increases downward and Doppler increases to the right, so rotation is counterclockwise. The spin vector is shown as an arrow in the plane-of-sky views. From top to bottom, the rows are in order of increasing rotation phase (increasing west longitude, decreasing east longitude); see Table 2.

Kleopatra images to obtain what we considered to be, and has been demonstrated to be (Hestroffer et al., 2002; Marchis et al., 2008), a reliable shape solution.

6. Southern hemisphere topography

Despite these difficulties in estimating Iris' global shape, all of our experiments with different initial conditions (including variations in the starting ellipsoid and the radar scattering law), penalty factors, step sizes, and convergence tolerances demonstrate convincing consistency in the topographic reconstruction of the southern region viewed by our data.

Our delay-Doppler images have 5.25-by-4-km resolution cells. As illustrated in Figs. 2–4, the model's southern hemisphere topography is dramatic, with concavities whose surface extents are typically of order 30–60 km and whose depths with respect to Iris' convex envelope approach 20 km, or 10% of the object's diameter. The volume of the model's convex envelope is about 6% greater than that of the model. The geologic nature of the topography is hard to judge definitively, but the prominent concavities, including the three ~50-km ones almost equally spaced in longitude around the south pole (“view from $-z$ ” in Fig. 3), are obviously prime candidates for impact craters.

7. Discussion

As illustrated in Fig. 5, Iris is much smaller than the Dawn Mission targets 4 Vesta and 1 Ceres but much larger than asteroids already imaged by flyby or rendezvous spacecraft. Its maximum dimension is comparable to Kleopatra's, but Kleopatra is in the M class and probably is metallic, with an exotic shape, whereas Iris is basically an ellipsoidal S-class object. Its shape is certainly not exotic, and its relief, although considerable, is not as dramatic as that seen on the smaller objects in the figure, which display very large fractional deviations from an ellipsoid. Yet the relief on Ceres

and Vesta is less dramatic still; even the latter object's 13-km-deep southern impact basin with its 13-km-high central peak is only 2.5% of Vesta's effective diameter (Thomas et al., 1997). Hence our impression is that in terms of shape regularity and fractional relief, Iris is a plausible, perhaps even canonical, ~200-km transition object between asteroids <50 km with extremely irregular overall shapes and very large concavities and the handful of asteroids ≥ 500 km with very regular, nearly convex shapes and generally lacking monumental concavities.

Studies of the effects of collisions on asteroid shapes and spins (Davis et al., 1979, 1989) suggest that most asteroids with diameters as large as 100 km are probably thoroughly fractured, gravitationally-bound rubble piles (Richardson et al., 2002). Farinella et al. (1982) considered effects of the most energetic collisions likely to have occurred over Solar System history and concluded that the largest asteroids may have retained their primordial masses and spin rates, and that asteroids in the 150–300 km size range may have been mostly shattered, with the fragments re-accumulated into quasi-equilibrium shapes. These inferences appear compatible with Iris' physical properties.

Not only size but also bulk density may influence an object's collisional evolution. When combined with Pitjeva's (2005) estimate of Iris' mass, $(12.5 \pm 0.188) \times 10^{21}$ g, our radar-derived volume constraint for Iris (see Table 1) corresponds to a density of $2.66 (+2.55, -0.87)$ g cm $^{-3}$. Despite the large uncertainty, it is worth noting the estimate's proximity to the spacecraft-derived values for the S-class asteroids 433 Eros (2.67 ± 0.03 g cm $^{-3}$, Yeomans et al., 2000) and 243 Ida (2.6 ± 0.5 g cm $^{-3}$, Belton et al., 1995). Based on the mean bulk density of ordinary chondrite meteorites, 3.34 g cm $^{-3}$ (Consolmagno et al., 1998), the nominal macroporosity of Iris is between 7% and 37%, placing it within the “fractured” group of asteroids defined by Britt et al. (2002) or, perhaps, in the transition zone that leads to “rubble piles.” Britt et al. point out that although the distinction between rubble piles, fractured asteroids, and “coherent” (zero macroporosity) objects tends to be one of size, there are exceptions; for example, Ida is an-

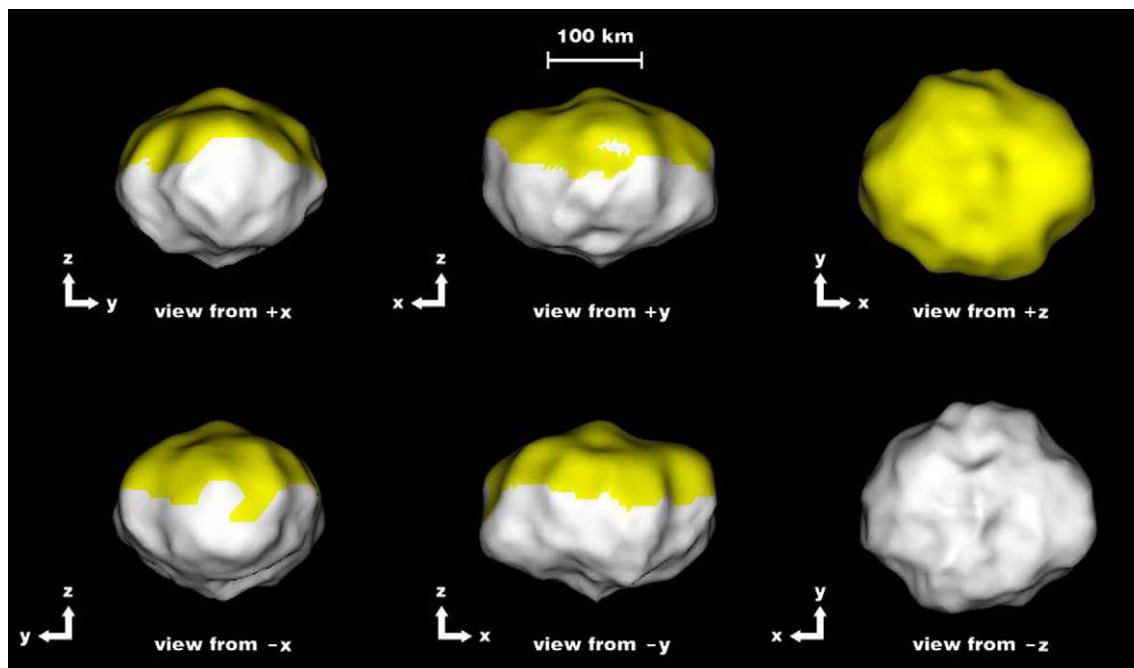


Fig. 3. Principal-axis views of our Iris model. The region colored yellow (essentially the northern hemisphere) was never seen by the radar at angles of incidence less than 60° and hence made weak or nonexistent contributions to the received signal; therefore this part of the model has minimal accuracy, and the dimension of the model normal to its equator has large uncertainty (Table 1).

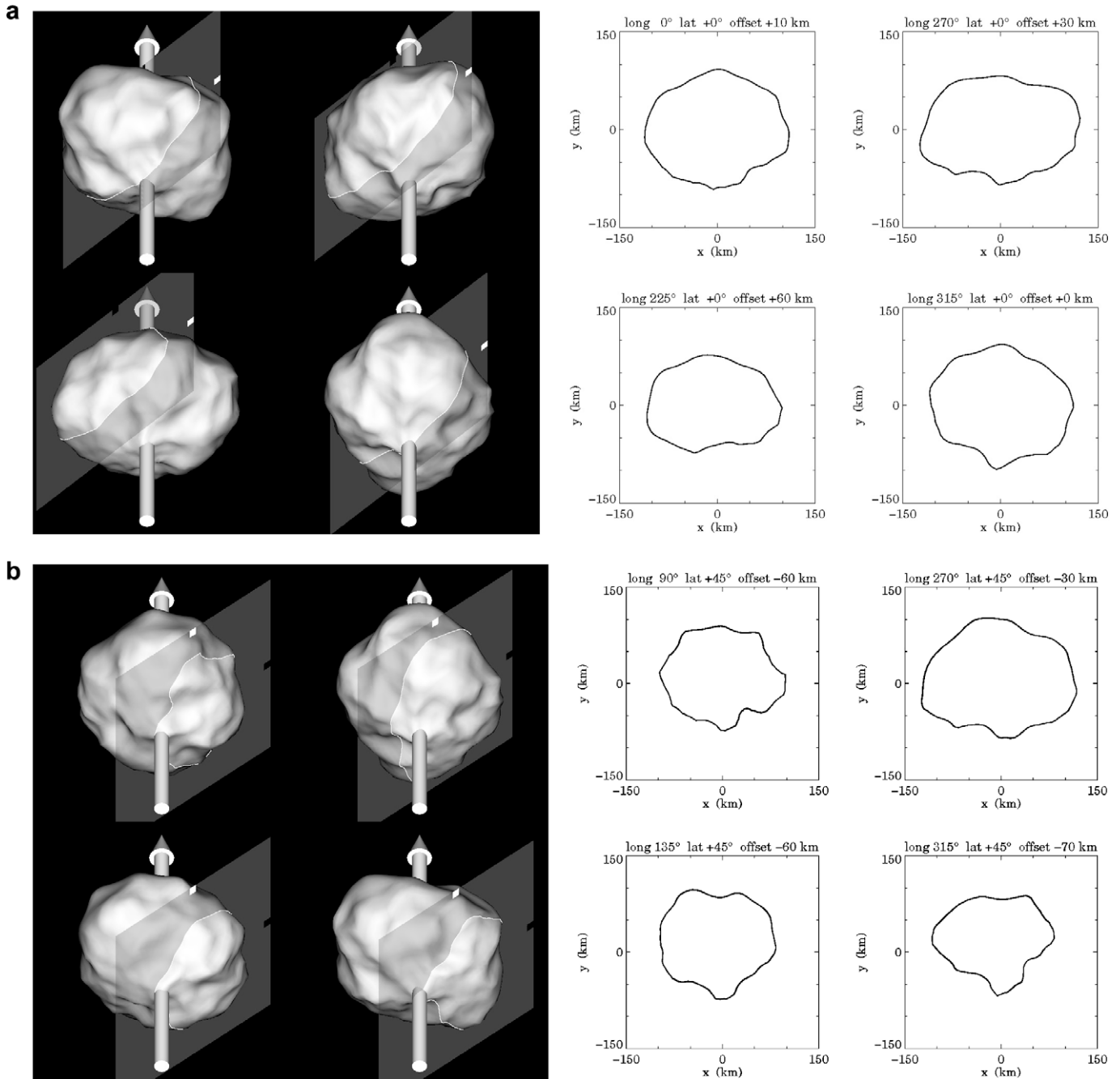


Fig. 4. Contours defined by the intersections of planes with our model's surface. The location and orientation of the slicing plane is defined by the latitude and east longitude of the plane's outward normal and by the plane's offset along that normal from the model's centre of mass. The slicing planes in Fig. 4a have equatorial normals (latitude = 0°) and the slicing planes in Fig. 4b have normals at latitude = +45°. Fig. 4a and b each contain two four-frame collages: (left) a collage that renders the slicing plane's cut through the model and (right) a face-on view of the intersection contour on a linear scale. The +x and +y axes in each face-on view correspond to the small white and black squares, respectively, shown in the left-hand collage. In each four-frame collage of Fig. 4a, the slicing plane's outward normal is at longitude 0° and 225° from top to bottom in the left column and 270° and 315° from top to bottom in the right column; the corresponding values for Fig. 4b are 90° and 135° in the left column and 270° and 315° in the right column. In the left four-frame collages of Fig. 4a and b, the scene is viewed above latitude -50° (approximately the subradar latitude of our imaging) and a longitude 45° greater than the longitude of the slicing plane's outward normal. The arrows in the left-hand collages denote the spin vector.

other fractured main-belt asteroid despite being much smaller than Iris (see Fig. 5), and the three large coherent asteroids (Ceres, Vesta, and 2 Pallas) are joined by the far smaller object 20 Massalia. This stochasticity, the accidental details of each object's collisional history, also plays a role.

Our shape estimation shows no evidence for craters with diameters comparable to or larger than Iris' average radius, in contrast with the several spacecraft-imaged asteroids that do have at least one such crater (Thomas et al., 1999), the most striking example of

which is 253 Mathilde (Cheng and Barnouin-Jha, 1999). Asphaug (2008) defines the critical crater diameter D_{crit} as the smallest crater whose formation disrupts all previous craters globally up to its size. He suggests that D_{crit} is related to the interaction between crater growth and stress attenuation in an impact. For a given value of stress wave attenuation, $\chi \equiv D_{crit}/D$ increases with asteroid diameter D . Asphaug notes that large asteroids can have giant under-graded craters, and D_{crit} can even exceed D , in which case all craters are "local" and the asteroid becomes crowded with giant

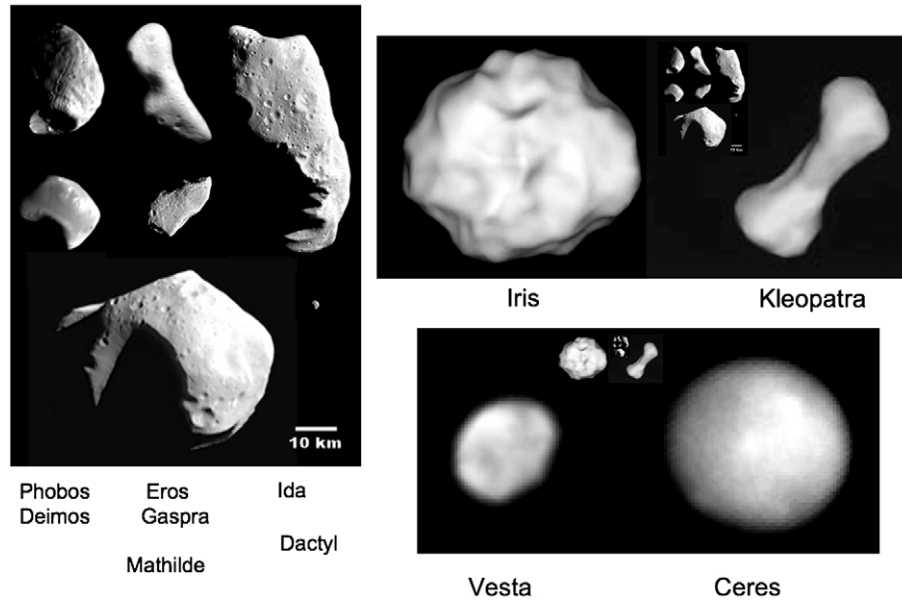


Fig. 5. Our Iris model and the (Ostro et al., 2000) Kleopatra model shown in proper size relationship to Ceres and Vesta (from Hubble images) and to a collage of asteroids imaged by spacecraft (patterned on Fig. 1 of Sullivan et al. (2002)).

craters. While we do not have information on Iris' northern hemisphere, there are features in our model that are plausibly well-defined craters that are 50–100 km across, giving $\chi \sim 0.2$ –0.4. Looking at the parameters listed for various objects in Table 1 of Asphaug (2008), we find that the size and density d of Iris are bracketed by those of the jovian satellite Amalthea ($D = 167$ km, $d = 0.86$ g cm $^{-3}$, $\chi = 0.52$) and Vesta ($D = 530$ km, $d = 3.5$ g cm $^{-3}$, $\chi = 0.85$). Since Iris is intermediate between these two, we might have expected to find that it has $\chi \geq 0.6$; the fact that we actually obtain a lower value suggests that Iris' material attenuates shock waves somewhat less well than Amalthea and Vesta, or else that we have failed to discern larger craters in the poorly covered

northern hemisphere. With the limited number of imaged objects, however, we should not be surprised to frequently discover new kinds of objects that do not follow established trends. To say more than this we must first improve our density estimate for Iris by observing it again, thus obtaining a better volume estimate by better constraining our model's northern hemisphere.

Table 3 shows that future high-SNR opportunities to refine our model of Iris' southern hemisphere come at roughly 11-year intervals. In fact, the far-southern viewing geometry for some of these apparitions contributes to the SNR, which is inversely proportional to the square root of $\cos(\text{LAT})$. Progress in constraining the northern hemisphere's topography, on the other hand, will be slower: views within a few tens of degrees of the equator yield moderate SNR for the reason just given, and views closer to the north pole occur at such large geocentric distances that those apparitions are too weak even to appear in the table. In January 2011 we hope to begin this project of obtaining the data needed for a globally accurate shape model of Iris.

Table 3
Iris radar opportunities, 2009–2100.

| Date | RA, Declination ($^{\circ}$) | Subradar latitude ($^{\circ}$) | Distance (AU) | Maximum SNR/date | |
|------|--------------------------------------|--|------------------|---------------------|-----|
| 2011 | January 13 | 128, +12 | +23 | 1.172 | 100 |
| 2017 | November 2 | 31, +21 | −64 | 0.849 | 590 |
| 2022 | January 3 | 117, +16 | +13 | 1.094 | 150 |
| 2028 | October 21 | 13, +16 | −74 | 0.879 | 670 |
| 2032 | December 23 | 104, +19 | 0 | 1.012 | 190 |
| 2039 | September 29 | 359, +12 | −73 | 0.934 | 460 |
| 2043 | December 12 | 89, +23 | −14 | 0.937 | 280 |
| 2050 | September 16 | 346, +6 | −62 | 1.002 | 240 |
| 2054 | November 30 | 72, +24 | −29 | 0.883 | 370 |
| 2061 | August 30 | 336, +1 | −53 | 1.083 | 110 |
| 2065 | November 18 | 55, +24 | −43 | 0.853 | 450 |
| 2076 | November 6 | 37, +22 | −59 | 0.849 | 550 |
| 2081 | January 6 | 121, +15 | +16 | 1.111 | 140 |
| 2087 | November 5 | 17, +16 | −72 | 0.895 | 590 |
| 2091 | December 27 | 108, +18 | +4 | 1.025 | 180 |
| 2098 | October 3 | 3, +13 | −75 | 0.924 | 510 |

Note: Radar apparitions between 2009 and 2100 for which the predicted OC signal-to-noise ratio (SNR) per date for CW measurements at Arecibo reaches 100 or greater. Listed quantities are the UT date of maximum SNR per date; the target's right ascension, declination, subradar latitude, and distance from Earth on that date; and the maximum OC SNR per date. We assume typical Arecibo observing parameters: sensitivity 10 K/Jy, system temperature 25 K, and transmitted power 900 kW. We also assume an OC radar albedo of 0.13 for Iris (Magri et al., 2007a), and we take into account the increase in SNR that results from viewing at high subradar latitude. For comparison, the maximum SNR per date predicted for the 2006 radar experiment was 490.

Acknowledgements

We thank the Arecibo technical and support staffs for help with the radar observations. The Arecibo Observatory is part of the National Astronomy and Ionosphere Center, which is operated by Cornell University under a cooperative agreement with the National Science Foundation (NSF). We thank M. Kaasalainen for kindly providing information regarding the Iris lightcurve data set, E. Asphaug for helpful discussions, and an anonymous reviewer and I. de Pater for constructive reviews that improved the presentation of this work. C. Magri was partially supported by NSF Grant AST-0205975. Some of this work was performed at the Jet Propulsion Laboratory, California Institute of Technology, under contract with the National Aeronautics and Space Administration (NASA). This material is based in part upon work supported by NASA under the Science Mission Directorate Research and Analysis Programs.

Appendix A. Long-code observations and data reduction

Magri et al. (2007b; see Appendix A) discussed in some detail observing procedure, data reduction, noise statistics, and signal

calibration for delay-Doppler imaging of NEAs. In order to maximize the average power, a continuous wave is transmitted rather than a series of brief pulses, but this means that the echo received at any given instant is a sum of contributions from power that scattered from different parts of the target's surface at different distances from Earth. We solve this problem (i.e., achieve delay resolution) by using a repeating pseudorandom binary phase code to modulate the transmitted sinusoid. The received signal (voltage time series) is decoded by cross-correlating it with a copy of the code; this procedure retains only the desired echo contributions, as it is a property of these codes that their autocorrelation function is similar to a delta function (Evans, 1968; Section 9-2B). The decoded signal at each delay lag (image row) is then Fourier-transformed to produce a Doppler spectrum.

There are some negative side effects of this approach. The resulting image does not provide delay values in the absolute sense but only modulo the code's repetition time, so at the outset of an experiment, when ephemeris uncertainties exceed this repetition time, further observations must be undertaken to resolve this delay ambiguity. Another side effect is that cross-correlation in the time domain shows up as multiplication by a sinc-squared function in the frequency domain: a "code filter" $Y(f)$, representing a slow sensitivity falloff with Doppler frequency f on either side of 0 Hz. Finally, and potentially most importantly, if the product of a target's delay depth and its Doppler bandwidth exceeds unity, the target is "overspread" and some fraction of its signal will be "aliased" – that is, will show up in the image at the wrong delay or the wrong Doppler frequency.

Overspreading usually is not a concern for NEA radar experiments: these targets are small, and both delay depth and Doppler bandwidth are directly proportional to target diameter. But it can be a problem for MBA observations, since the inverse-fourth-power falloff of echo power with distance means that these distant targets must be large if we are to have any hope of imaging them. Even if an MBA is not quite overspread, the sensitivity falloff away from 0 Hz means that signal from near the target's limbs may be lost in the noise.

Hence we employ the "coded long pulse" or "long code" method for delay-Doppler imaging of MBAs. This method, which uses a non-repeating pseudorandom binary phase code to modulate the transmitted continuous wave, was devised for ionospheric radar observations (Sulzer, 1986, 1989) and was first applied to planetary targets during radar imaging of Mars by Harmon et al. (1992). Rather than decoding the received signal by cross-correlating it with a copy of the code and then Fourier-transforming the decoded signal at each delay lag to produce a Doppler spectrum, we process each delay lag separately, forming a product of the received signal with a suitably lagged (shifted) copy of the code and then Fourier-transforming that product to obtain the Doppler spectrum for that lag. Each of these spectra contains power contributions from the "wrong" lags, but this power is effectively diluted, spread out across the entire Doppler bandwidth as a plateau of "clutter noise." For a strong target like Mars, one subtracts off this plateau before proceeding with the analysis; for the much weaker echoes from Iris, clutter noise was insignificant enough to ignore. The images generally have curved Doppler bandpasses, so we estimate and then remove this curvature by looking at the portion of the image that does not contain any signal from the target.

The long-code method produces delay-Doppler images that are free from delay and Doppler aliasing, even for overspread targets. Furthermore, since data reduction does not involve cross-correlation with a repeating code, there is no sensitivity falloff away from 0 Hz. The primary drawback to the method is that data reduction is a slow process. With a repeating code, one can speed things up by Fourier-transforming the code and then invoking the convolution theorem to replace cross-correlation in the time domain by simple

multiplication in the frequency domain. No such shortcut is possible with the long code, so it can happen that our images are not available for inspection until hours after we have finished observing for the night.

Harmon (2002) provides expressions for long-code noise statistics and signal calibration for the case of data taking at a rate of one complex voltage sample per baud. (The baud is the phase modulation interval, the time over which each code element is applied to the transmitted signal.) Our Iris data were taken at two samples per baud, which complicates the analysis. Magri et al. (2007b) provide analogous expressions (in their Appendix A) for repeating-code data with multiple samples per baud, and these formulae are still valid for long-code data so long as one replaces the code filter $Y(f)$ with unity throughout. Magri et al. do *not* analyze clutter noise but, as was already mentioned, this was an unimportant factor for our Iris images.

References

- Andrews, A.K., Hudson, R.S., Psaltis, D., 1995. Optical-radar imaging of scale models for studies in asteroid astronomy. *Opt. Lett.* 20, 2327–2329.
- Asphaug, E., 2008. Critical crater diameter and asteroid impact seismology. *Meteorit. Planet. Sci.* 43, 1075–1084.
- Belton, M., and 12 colleagues, 1995. Bulk density of Asteroid 243 Ida from the orbit of its satellite Dactyl. *Nature* 374, 785–788.
- Britt, D.T., Yeomans, D., Housen, K., Consolmagno, G., 2002. Asteroid density, porosity, and structure. In: Bottke, W.F., Cellino, A., Paolicchi, P., Binzel, R.P. (Eds.), *Asteroids III*. University of Arizona Press, Tucson, pp. 485–500.
- Brogia, P., Manara, A., 1990. A search for rotational variations in the optical polarization of 3 Juno and 7 Iris. *Astron. Astrophys.* 237, 256–258.
- Cheng, A.F., Barnouin-Jha, O.S., 1999. Giant craters on Mathilde. *Icarus* 140, 34–48.
- Consolmagno, G.J., Britt, D.T., Stoll, C.P., 1998. The porosities of ordinary chondrites: Models and interpretations. *Meteorit. Planet. Sci.* 33, 1221–1229.
- Davis, D.R., Chapman, C.R., Greenberg, R., Harris, A.W., 1979. Collisional evolution of asteroids: Populations, rotations, and velocities. In: Gehrels, T. (Ed.), *Asteroids*. University of Arizona Press, Tucson, pp. 528–557.
- Davis, D.R., Weidenschilling, S.J., Farinella, P., Paolicchi, P., Binzel, R.P., 1989. Asteroid collisional histories: Effects on sizes and spins. In: Binzel, R.P., Gehrels, T., Matthews, M.S. (Eds.), *Asteroids II*. University of Arizona Press, Tucson, pp. 805–826.
- de Pater, I., Palmer, P., Mitchell, D.L., Ostro, S.J., Yeomans, D.K., Snyder, L.E., 1994. Radar aperture synthesis observations of asteroids. *Icarus* 111, 489–502.
- Evans, J.V., 1968. Modulation, demodulation, and data processing applied to radar astronomy. In: Evans, J.V., Hagfors, T. (Eds.), *Radar Astronomy*. McGraw-Hill, New York, pp. 499–545.
- Farinella, P., Paolicchi, P., Zappalà, V., 1982. The asteroids as outcomes of catastrophic collisions. *Icarus* 52, 409–433.
- Farinella, P., Gonczi, R., Froeschlé, Ch., Froeschlé, C., 1993. The injection of asteroid fragments into resonances. *Icarus* 101, 174–187.
- Gaffey, M.J., Bell, J.F., Brown, R.H., Burbine, T.H., Piatek, J.L., Reed, K.L., Chaky, D.A., 1993. Mineralogical variations within the S-type asteroid class. *Icarus* 106, 573–602.
- Gaffey, M.J., Cloutis, E.A., Kelley, M.S., Reed, K.L., 2002. Mineralogy of asteroids. In: Bottke, W.F., Cellino, A., Paolicchi, P., Binzel, R.P. (Eds.), *Asteroids III*. University of Arizona Press, Tucson, pp. 183–204.
- Harmon, J.K., 2002. Planetary delay-Doppler radar and the long-code method. *IEEE Trans. Geosci. Remote Sens.* 40, 1904–1916.
- Harmon, J.K., Sulzer, M.P., Perillat, P.J., Chandler, J.F., 1992. Mars radar mapping: Strong backscatter from the Elysium basin and outflow channel. *Icarus* 95, 153–156.
- Hestroffer, D., Marchis, F., Fusco, T., Berthier, J., 2002. Adaptive optics observations of Asteroid (216) Kleopatra. *Astron. Astrophys.* 394, 339–343.
- Hoffmann, M., Geyer, E.H., 1993. Spots on (4) Vesta and (7) Iris: Large areas or little patches? *Astron. Astrophys. Suppl. Ser.* 101, 621–627.
- Hudson, R.S., Ostro, S.J., 1994. Shape of Asteroid 4769 Castalia (1989 PB) from inversion of radar images. *Science* 263, 940–943.
- Kaasalainen, M., Torppa, J., Piironen, J., 2002. Models of twenty asteroids from photometric data. *Icarus* 159, 369–395.
- Magri, C., Ostro, S.J., Rosema, K.D., Thomas, M.L., Mitchell, D.L., Campbell, D.B., Chandler, J.F., Shapiro, I.I., Giorgini, J.D., Yeomans, D.K., 1999. Mainbelt asteroids: Results of Arecibo and Goldstone radar observations of 37 objects during 1980–1995. *Icarus* 140, 379–407.
- Magri, C., Nolan, M.C., Ostro, S.J., Giorgini, J.D., 2007a. A radar survey of main-belt asteroids: Arecibo observations of 55 objects during 1999–2003. *Icarus* 186, 126–151.
- Magri, C., Ostro, S.J., Scheeres, D.J., Nolan, M.C., Giorgini, J.D., Benner, L.A.M., Margot, J.-L., 2007b. Radar observations and a physical model of Asteroid 1580 Betulia. *Icarus* 186, 152–177.
- Marchis, F., Descamps, P., Berthier, J., Emery, J.P., 2008. S/2008 (216) 1 and S/2008 (216) 2. *IAU Circular* 8980.

- Migliorini, F., Manara, A., Cellino, A., Di Martino, M., Zappalà, V., 1997. (7) Iris: A possible source of ordinary chondrite meteorites? *Astron. Astrophys.* 321, 652–659.
- Mitchell, D.L., Ostro, S.J., Rosema, K.D., Hudson, R.S., Campbell, D.B., Chandler, J.F., Shapiro, I.I., 1995. Radar observations of Asteroids 7 Iris, 9 Metis, 12 Victoria, 216 Kleopatra, and 654 Zelinda. *Icarus* 118, 105–131.
- Mitchell, D.L., Ostro, S.J., Hudson, R.S., Rosema, K.D., Campbell, D.B., Vélez, R., Chandler, J.F., Shapiro, I.I., Giorgini, J.D., Yeomans, D.K., 1996. Radar observations of Asteroids 1 Ceres, 2 Pallas, and 4 Vesta. *Icarus* 124, 113–133.
- Ostro, S.J., Hudson, R.S., Nolan, M.C., Margot, J.-L., Scheeres, D.J., Campbell, D.B., Magri, C., Giorgini, J.D., Yeomans, D.K., 2000. Radar observations of Asteroid 216 Kleopatra. *Science* 288, 836–839.
- Ostro, S.J., Hudson, R.S., Benner, L.A.M., Giorgini, J.D., Magri, C., Margot, J.-L., Nolan, M.C., 2002. Asteroid radar astronomy. In: Bottke, W.F., Cellino, A., Paolicchi, P., Binzel, R.P. (Eds.), *Asteroids III*. University of Arizona Press, Tucson, pp. 151–168.
- Ostro, S.J., and 12 colleagues, 2005. Radar observations of Itokawa in 2004 and improved shape estimation. *Meteorit. Planet. Sci.* 40, 1563–1574.
- Parker, M.N., 1973. Radio-wave Scattering from Rough Surfaces and the Estimation of Surface Shape. Ph.D. Dissertation, Stanford University, Stanford, CA.
- Pitjeva, E.V., 2005. High-precision ephemerides of planets—EPM and determination of some astronomical constants. *Solar Syst. Res.* 39, 176–186. Translated from *Astronomicheskii Vestnik*, vol. 39, No. 3, 2005, pp. 202–213.
- RASNZ, 2006: Royal Astron. Soc. New Zealand. <http://ocsec.wellington.net.nz/planet/2005/results/050217_Iris.htm>.
- Richardson, D.C., Leinhardt, Z.M., Melosh, H.J., Bottke Jr., W.F., Asphaug, E., 2002. Gravitational aggregates: Evidence and evolution. In: Bottke, W.F., Cellino, A., Paolicchi, P., Binzel, R.P. (Eds.), *Asteroids III*. University of Arizona Press, Tucson, pp. 501–515.
- Shepard, M.K. and 19 colleagues, 2008. A radar survey of M- and X-class asteroids. *Icarus* 195, 184–205.
- Simpson, R.A., Tyler, G.L., 1982. Radar scattering laws for the lunar surface. *IEEE Trans. Antennas Propag.* AP-30 (3), 438–449.
- Sullivan, R.J., Thomas, P.C., Murchie, S.L., Robinson, M.S., 2002. Asteroid geology from Galileo and NEAR Shoemaker data. In: Bottke, W.F., Cellino, A., Paolicchi, P., Binzel, R.P. (Eds.), *Asteroids III*. University of Arizona Press, Tucson, pp. 331–350.
- Sulzer, M.P., 1986. A radar technique for high range resolution incoherent scatter autocorrelation function measurements utilizing the full average power of klystron radars. *Radio Sci.* 21, 1033–1040.
- Sulzer, M.P., 1989. Recent incoherent scatter techniques. *Adv. Space Res.* 9, 153–162.
- Tedesco, E.F., Noah, P.V., Noah, M., Price, S.D., 2002. The Supplemental IRAS Minor Planet Survey. *Astron. J.* 123, 1056–1085.
- Thomas, P.C., Binzel, R.P., Gaffey, M.J., Storrs, A.D., Wells, E.N., Zellner, B.H., 1997. Impact excavation on Asteroid 4 Vesta: Hubble Space Telescope results. *Science* 277, 1492–1495.
- Thomas, P.C., and 11 colleagues, 1999. Mathilde: Size, shape, and geology. *Icarus* 140, 17–27.
- Turtle, E.P., and 19 colleagues, 1999. AMBASSADOR: Asteroid Sample Return Mission to 7 Iris. *Acta Astronaut.* 45, 415–422.
- Vernazza, P., Binzel, R.P., Thomas, C.A., DeMeo, F.E., Bus, S.J., Rivkin, A.S., Tokunaga, A.T., 2008. Compositional differences between meteorites and near-Earth asteroids. *Nature* 454, 858–860.
- Yeomans, D.K., and 15 colleagues, 2000. Radio science results during the NEAR-Shoemaker spacecraft rendezvous with Eros. *Science* 289, 2085–2088.